mathematics

MDPI

Article

A Non-Newtonian Magnetohydrodynamics (MHD) Nanofluid Flow and Heat Transfer with Nonlinear Slip and Temperature Jump

Jing Zhu *, Yaxin Xu and Xiang Han

School of Mathematics and Physics, University of Science and Technology Beijing, Beijing 100080, China; S20180748@xs.ustb.edu.cn (Y.X.); S20170736@xs.ustb.edu.cn (X.H.)

* Correspondence: zhujing@ustb.edu.cn; Tel.: +86-1368-121-2703

Received: 29 August 2019; Accepted: 28 November 2019; Published: 6 December 2019

Abstract: The velocity and thermal slip impacts on the magnetohydrodynamics (MHD) nanofluid flow and heat transfer through a stretched thin sheet are discussed in the paper. The no slip condition is substituted for a new slip condition consisting of higher-order slip and constitutive equation. Similarity transformation and Lie point symmetry are adopted to convert the derived governed equations to ordinary differential equations. An approximate analytical solution is gained through the homotopy analysis method. The impacts of velocity slip, temperature jump, and other physical parameters on flow and heat transfer are illustrated. Results indicate that the first-order slip and nonlinear slip parameters reduce the velocity boundary layer thickness and Nusselt number, whereas the effect on shear stress is converse. The temperature jump parameter causes a rise in the temperature, but a decline in the Nusselt number. With the increase of the order, we can get that the error reaches 10^{-6} from residual error curve. In addition, the velocity contours and the change of skin friction coefficient are computed through Ansys Fluent.

Keywords: velocity-slip; temperature-jump; homotopy analysis method; nanofluids; power-law fluids

1. Introduction

In a heat transfer mechanism, fluid is a main medium as a heat transfer carrier. Therefore, improving the thermal transfer efficiency of the fluid used is a vital challenge in the industry. Certain experiments have shown that the thermal conductivity of fluids containing metal and oxide particles is higher than that of traditional base liquids such as oil, water, and ethylene glycol [1–3]. For the sake of improving the heat transfer efficiency of the fluid, researchers have added metal and non-metallic nanoparticles into the traditional base liquid to form a new compound "nanofluid". Nanofluids are made up of base fluids and nanoparticles, but not a simple mixture, which are composed of nano-sized solid particle or tubes suspended in the base fluids, are solid–liquid composite materials. Nanoparticles have high surface-activity and tend to aggregate together with time. The idea was first proposed by Choi and Eastman [4]. Nanofluids are important in the fields of energy, chemical, microelectronics, and information. Recently, the flow and conduct heat of nanofluids have been studied by certain scholars. A quick overview is given here. Sheremet et al. [5] discussed natural convection of alumina-water nanofluid in an inclined wavy-walled cavity. Nanofluids flow in microchannels with heat conduction was discussed by Bowers et al. [6]. Hashim et al. [7] discussed the mixed convection and heat conduction of Williamson nanofluids under unsteady condition. Mahdy [8] presented the effects of magnetohydrodynamics (MHD) and variable wall temperature on non-Newtonian Casson nanofluid flow. Asadi et al. [9] presented the latest progress of preparation methods and thermophysical properties of oil-based nanofluids. Pourfattah et al. [10] simulated water/CuO

nanofluid fluid flow and heat transfer inside a manifold microchannel. Alarifi et al. [11] investigated the effects of solid concentration of nanoparticles, temperature, and shear rate on the rheological properties of nanofluid. For a traditional base fluid, there are two main types: Newtonian fluids and non-Newtonian fluids. In industry, non-Newtonian fluids play an important role, such as juices, starch solutions, egg whites, and apple pulp. To understand behavious of non-Newtonian fluids, certain models have been presented. Power law model is relatively simple, widely used among these models. Researchers have further investigated the flow and conduct heat of power law fluids. Javanbakht et al. [12] studyed the heat conduction on the surface of a power law fluid. Turan et al. [13] discussed mixed convection of power-law liquids in enclosures. The heat conduction of power law liquid in various section tubes was considered by Zhang et al. [14]. Ahmedet et al. [15] addressed MHD power law liquid flow in a Darcy–Brinkmann porous medium.

In this paper, the base fluid of a nanofluid is power law fluid. When nanoparticles are added into the traditional base liquid, local velocity slip may happen as an effect of high shear force between the fluid and the wall, and the slip condition is no longer negligible in the nanometer or micro scales. The velocity slip is a finite velocity boundary condition between the fluid and the solid [16]. Researchers have done certain studies on the slipping problems of nanofluids. Ramya et al. [17] studied the viscous flow and heat transfer of nanofluid through a stretched sheet with the effect of magnetic field, velocity, and thermal slip. Abbas et al. [18] discussed the stagnation flow of micropolar nanofluids through a cylinder with slip. The effect of heat and velocity slip on the flow of Carson nanofluids through a cylinder was discussed by Usman et al. [19]. Babu et al. [20] investigated the three-dimensional MHD nanofluid flow over a variable thickness slendering stretching sheet with the effect of thermophoresis, Brownian motion, and slip parameter. The above studies all discussed the first-order slip model, whereas higher-order slips should be considered when the velocity and temperature profiles of an average free path are nonlinear. It is now known that the inclusion of higher-order slip yields results closer to those by experiments [21]. Thus, various investigations on higher-order slip flows were published by Uddin et al. [22], Kamran et al. [23], Farooq et al. [24], and Yasin et al. [25]. These all suggest that the power law constitutive equation should be considered on the basis of high order slip for a power law nanofluid.

In the aforementioned literature, there are few papers about the flow and heat transfer of magnetic nanofluids with higher-order slip parameters. Therefore, a new mathematical model is proposed. With the help of similarity transformation variables, governing equations are converted to ordinary differential equations, whose solution is solved using homotopy analysis method. The effects of nanofluid velocity, temperature, concentration, skin friction coefficient and Nusselt number on various physical parameters are simulated. In addition, the fluid flow situation is visualized by the computational fluid dynamics (CFD) software Ansys Fluent.

2. Mathematical Modelling Formulation

2.1. Flow Behavior

Consider a steady, two-dimensional, incompressible MHD fluid flow with copper through a stretching thin plate. All variables mentioned are presented in Tables 1 and 2 [26] gives some physical capabilities of the base liquid and nanoparticles. Meanwhile, a transverse magnetic field is utilized, where the strength is B_x and the presence of surface tension is also considered. Given the above hypotheses, the governing equations composed of continuity equation and momentum equation can be given as

$$\frac{\partial U}{\partial X} + \frac{\partial V}{\partial Y} = 0, \tag{1}$$

$$U\frac{\partial U}{\partial X} + V\frac{\partial U}{\partial Y} = -\frac{1}{\rho_{nf}}\frac{\partial P}{\partial X} + \frac{\partial S_{XX}}{\partial X} + \frac{\partial S_{XY}}{\partial Y} + \frac{\sigma B^2}{\rho_{nf}}(U_e - U), \tag{2}$$

$$U\frac{\partial V}{\partial X}+V\frac{\partial V}{\partial Y}=-\frac{1}{\rho_{nf}}\frac{\partial P}{\partial Y}+\frac{\partial S_{YX}}{\partial X}+\frac{\partial S_{YY}}{\partial Y}, \tag{3}$$

$$S_{ij}=2\mu_{nf}\left(2D_{ml}D_{ml}\right)^{\frac{n-1}{2}}D_{ij}, D_{ij}=\frac{1}{2}\left(\frac{\partial \mathbf{U}_i}{\partial \mathbf{X}_j}+\frac{\partial \mathbf{U}_j}{\partial \mathbf{X}_i}\right). \tag{4}$$

Table 1. Nomenclature.

Symbol	Description	Symbol	Description
B_x	magnetic field strength	c_p	heat capacity
$\mathbf{U}$	field velocity	U_e	free stream speed
T	temperature in the boundary layer	T_∞	temperature far away from the sheet
T_w	unified temperature	C	concentration
C_∞	fluid concentration in the free stream	C_w	unified concentration
S_{ij}	deviatoric part of the stress tensor	δ_{ij}	unit tensor
D_{ij}	rate-of-strain tensor	σ	electrical conductivity
D_T	thermophoresis diffusion coefficient	$\lambda_1, \lambda_2, \lambda_3$	slip parameters of velocity
φ	nanoparticle volume fraction	ρ	density
α	thermal diffusivity	k	thermal conductivity
P	pressure	μ	dynamic viscosity
Nu	Nusselt number	C_f	skin friction coefficients
Pr	Prandtl number	Nt	thermophoresis parameter
Nb	Brownian motion parameter	Sc	Schmidt number
M	Hartmann number	Re	Reynolds number
D_B	Brownian diffusion	Sh	Sherwood number
f	fluid phase	s	solid phase
nf	nanofluid	η	similarity variable
U, V	velocity components	X, Y	Cartesian coordinates

In the above, X and Y are the Cartesian coordinates along and normal to the extension sheet, respectively. $\mathbf{U}$ is the velocity field. U and V are the x and y components of $\mathbf{U}$. P is the pressure, σ the electric conductivity, B_x the magnetic field along the forward direction of Y-axis, U_e the free stream speed, S_{ij} the deviatoric part of the stress tensor $\varsigma_{ij}=-P\delta_{ij}+S_{ij}$, δ_{ij} the unit tensor, and D_{ij} the rate-of-strain tensor. ρ_{nf} the effective density and μ_{nf} the effective dynamic viscosity given by [27]

$$\rho_{nf}=(1-\varphi)\rho_f+\varphi\rho_s, \quad \mu_{nf}=\frac{\mu_f}{(1-\varphi)^{2.5}}. \tag{5}$$

The other parameters of nanofluid $(\rho C_p)_{nf}$, α_{nf}, k_{nf} are given [27]

$$(\rho C_p)_{nf}=(1-\varphi)(\rho C_p)_f+\varphi(\rho C_p)_s, \quad \alpha_{nf}=\frac{k_{nf}}{(\rho C_p)_{nf}}, \tag{6}$$

$$\frac{k_{nf}}{k_f}=\frac{k_s+2k_f-2\varphi(k_f-k_s)}{k_s+2k_f+\varphi(k_f-k_s)}, \tag{7}$$

where subscripts s, f, and nf represent the solid particle, base liquid, and the thermophysical properties of nanofluid, respectively. φ is the solid volume fraction of nanoparticles, $(\rho C_p)_{nf}$ the effective heat capacity. The thermal conductivity is k_{nf} and the thermal diffusivity is α_{nf}.

For the sake of analyzing the boundary layer in a better way, the following nondimensional variables are introduced,

$$x=\frac{X}{L}, y=\frac{Y}{\delta}, u=\frac{U}{U_w}, v=\frac{LV}{\delta U_w}, p=\frac{P}{\rho_f U_w^2}, \tau_{ij}=\frac{S_{ij}}{\rho_f U_w^2}, \tag{8}$$

where L and δ represent the characteristic length in the X and Y direction, respectively. U_w denotes the velocity in the X-direction.

Thus, Equations (1)–(4) become

$$\frac{\partial u}{\partial x} + \frac{\partial v}{\partial y} = 0, \tag{9}$$

$$u\frac{\partial u}{\partial x} + v\frac{\partial u}{\partial y} = -\frac{\rho_f}{\rho_{nf}}\frac{\partial p}{\partial x} + \frac{\partial}{\partial y}\left(\frac{\mu_{nf}\rho_f}{\rho_{nf}}\left|\frac{\partial u}{\partial y}\right|^{n-1}\frac{\partial u}{\partial y}\right) + \frac{\rho_f \sigma B^2}{\rho_{nf}}(u_e - u), \tag{10}$$

$$\frac{\partial p}{\partial y} = 0. \tag{11}$$

From Equation (11), it can be concluded that the pressure p is identical with the pressure of mainstream flow.

$$-\frac{\partial p}{\partial x} = u_e\frac{\partial u_e}{\partial x}. \tag{12}$$

For a power law nanofluid, velocity slip effect need be considered. In many investigations, the first-order model is adopted widely. The model is suitable under the assumption that temperature and velocity profiles are linear through a average free path. However, when temperature and velocity profiles are nonlinear through a average free path, higher-order slip would become possible. Mitsuya [28] has obtained a second-order slip model from a physical phenomenon by considering the accommodation coefficient:

$$F = \alpha f_1 m_1\left[\left(\frac{2}{3}\lambda\right)\frac{\partial u}{\partial y} + \frac{1}{2}\left(\frac{2}{3}\lambda\right)^2\frac{\partial^2 u}{\partial y^2} + u_{slip}\right]|_{y=0}, \tag{13}$$

where F is the shear stress, α an accommodation coefficient relative to momentum, f_1 the frequency of molecular bombardment, m_1 the molecular mass density, and λ the local molecular average free path.

In this paper, as the base fluid is a power flow fluid, namely, the shear stress $F = \mu_{nf}\left|\frac{\partial u}{\partial y}\right|^{n-1}\frac{\partial u}{\partial y}$, the constitutive equation of a power flow fluid with a higher-order slip is considered. The enhanced slip model is written as

$$u(x,0) = U_w + \left(A_1\frac{\partial u}{\partial y} + A_2\frac{\partial^2 u}{\partial y^2} + A_3\left|\frac{\partial u}{\partial y}\right|^{n-1}\frac{\partial u}{\partial y}\right)|_{y=0}, \tag{14}$$

$$v(x,0) = 0, u(x,\infty) = u_e = ax^m, \tag{15}$$

where A_1, A_2, and A_3 denote the velocity slip coefficients; U_w is the the speed of the stretch plate; and $U_w = cx^m$.

For the sake of deriving a simplified model by converting governing equations into ordinary differential equations, a stream function $\psi(x,y)$ is introduced in this paper such that $u = \frac{\partial \psi}{\partial y}, v = -\frac{\partial \psi}{\partial x}$. Then Lie-group transformationsis also introduced to obtain a new set of similar variables.

$$\Gamma : x^* = xe^{\varepsilon\alpha_1}, \quad y^* = ye^{\varepsilon\alpha_2}, \quad \psi^* = \psi e^{\varepsilon\alpha_3}, \quad u^* = ue^{\varepsilon\alpha_4}, \quad v^* = ve^{\varepsilon\alpha_5}, \quad u_e^* = u_e e^{\varepsilon\alpha_6}. \tag{16}$$

Equation (16) can be considered as a point-transformation of coordinates (x, y, ψ, u, v, u_e) into coordinates $(x^*, y^*, \psi^*, u^*, v^*, u_e^*)$. Substituting Equation (16) in Equation (10), we get

$$\begin{aligned} & e^{\varepsilon(\alpha_1+2\alpha_2-2\alpha_3)}\left(\frac{\partial\psi^*}{\partial y^*}\frac{\partial^2\psi^*}{\partial x^*\partial y^*}-\frac{\partial\psi^*}{\partial x^*}\frac{\partial^2\psi^*}{\partial y^{*2}}\right) \\ = \quad & -e^{\varepsilon(\alpha_1-2\alpha_6)}\frac{\rho_f}{\rho_{nf}}u_e^*\frac{du_e^*}{dx^*}+e^{\varepsilon(3\alpha_2-\alpha_3)}\frac{\mu_{nf}\rho_f}{\rho_{nf}}\frac{\partial^3\psi^*}{\partial y^{*3}}e^{\varepsilon(n-1)(2\alpha_2-\alpha_3)}\left(-\frac{\partial^2\psi^*}{\partial y^{*2}}\right)^{n-1} \\ + \quad & \frac{\rho_f\sigma B^2}{\rho_{nf}}\left(e^{-\alpha_6\varepsilon}u_e^*-e^{(\alpha_2-\alpha_3)\varepsilon}\frac{\partial\psi^*}{\partial y^*}\right). \end{aligned} \tag{17}$$

The boundary condition Equations (14) and (15) become

$$\begin{aligned} & \frac{\partial\psi^*}{\partial y^*}(x^*,0)=e^{\varepsilon(\alpha_3-\alpha_2-m\alpha_1)}cx^{*m}+A_1e^{\varepsilon\alpha_2}\frac{\partial^2\psi^*}{\partial y^{*2}}+A_2e^{\varepsilon\alpha_2}\frac{\partial^3\psi^*}{\partial y^{*3}} \\ + \quad & A_3e^{(n\varepsilon(2\alpha_2-\alpha_3)+\alpha_3-\alpha_2)}\left(-\frac{\partial^2\psi^*}{\partial y^{*2}}\right)^{n-1}\left(-\frac{\partial^2\psi^*}{\partial y^{*2}}\right), \quad at \quad y^*=0; \end{aligned} \tag{18}$$

$$\frac{\partial\psi^*}{\partial x^*}(x^*,0)=0, \quad at \quad y^*=0; \tag{19}$$

$$\frac{\partial\psi^*}{\partial y^*}(x^*,\infty)=e^{\varepsilon(\alpha_3-\alpha_2-m\alpha_1)}ax^{*m}, \quad at \quad y^*\to\infty. \tag{20}$$

The system will remain unaltered under the group of transformations Γ, so the parameters have the following relations, namely,

$$\alpha_2+\alpha_4-\alpha_3 = \alpha_1+\alpha_5-\alpha_3=\alpha_3-\alpha_1-m\alpha_2=\alpha_3-\alpha_2-m\alpha_1=0, \tag{21}$$

$$2\alpha_2-2\alpha_3+\alpha_1 = n(2\alpha_2-\alpha_3)+\alpha_2=(n+1)\alpha_2-n\alpha_4=\alpha_2-\alpha_4-\alpha_5. \tag{22}$$

Thus, Equation (16) becomes

$$\begin{aligned} \Gamma: \quad & x^*=xe^{\varepsilon\alpha_1}, \quad y^*=ye^{\frac{mn-2m+1}{n+1}\alpha_1\varepsilon}, \quad \psi^*=\psi e^{\frac{2mn-m+1}{n+1}\alpha_1\varepsilon}, \\ & u^*=ue^{m\alpha_1\varepsilon}, \quad v^*=ve^{\frac{2mn-m-n}{n+1}\alpha_1\varepsilon}. \end{aligned} \tag{23}$$

Based on the above Lie-group transformations, the stream function and similar parameter can be prescribed as follows,

$$\eta=\left(\frac{c^{2-n}}{\mu_f}\right)^{\frac{1}{n+1}}x^{\frac{2m-mn-1}{n+1}}y, \psi=\left(\frac{\mu_f}{c^{1-2n}}\right)^{\frac{1}{n+1}}x^{\frac{2mn+1-m}{n+1}}f(\eta). \tag{24}$$

After further similarity transformations, a nonlinear ordinary differential equation is obtained.

$$nf'''|f''|^{n-1}+m\varphi_1(d^2-f'f')+\varphi_1\varphi_2\frac{2mn-m+1}{n+1}ff''+\varphi_1M(d-f')=0. \tag{25}$$

The boundary condition Equations (14) and (15) now develop into

$$f(0)=0, f'(\infty)=d, \tag{26}$$

$$f'(0)=1+\lambda_1f''(0)+\lambda_2f'''(0)+\lambda_3\left|f''(0)\right|^{n-1}f''(0), \tag{27}$$

where $d=\frac{a}{c}$, M is the Hartmann number with $M=\frac{\sigma B_0^2}{c}$, λ_1,λ_2, and λ_3 are velocity slip parameters; these parameters and φ_1,φ_2 [27] can now be written as

$$\lambda_1 = A_1(\frac{c^{2-n}}{\mu_f})^{\frac{1}{n+1}} x^{\frac{2m-mn-1}{n+1}}, \lambda_2 = A_2(\frac{c^{2-n}}{\mu_f})^{\frac{2}{n+1}} x^{\frac{2(2m-mn-1)}{n+1}}, \tag{28}$$

$$\lambda_3 = A_3 \left(cx^m (\frac{c^{2-n}}{\mu_f})^{\frac{1}{n+1}} x^{\frac{2m-mn-1}{n+1}} \right)^n, \tag{29}$$

$$\varphi_1 = (1-\varphi)^{2.5}, \quad \varphi_2 = 1 - \varphi + \varphi \frac{\rho_s}{\rho_f}, \tag{30}$$

where A_1, A_2, and A_3 are arbitrary positive constants.

2.2. Heat and Mass Transfer Behavior

The heat and mass equations can now be formulated as follows,

$$\begin{aligned} U\frac{\partial T}{\partial X} + V\frac{\partial T}{\partial Y} = \frac{\partial}{\partial Y}\left(k(T)\frac{\partial T}{\partial Y}\right) \\ + \frac{\tau}{\mu_f} C_f \frac{3}{n+1}(C^3 x^{3m-1}) \frac{n-1}{n+1} \left(D_B \frac{\partial C}{\partial Y}\frac{\partial T}{\partial Y} + \frac{D_T}{T_\infty}\left(\frac{\partial T}{\partial Y}\right)^2 \right), \end{aligned} \tag{31}$$

$$U\frac{\partial C}{\partial X} + V\frac{\partial C}{\partial Y} = \mu_f{}^{\frac{2}{n+1}} (C^3 x^{3m-1})^{\frac{n-1}{n+1}} \left(D_B \frac{\partial^2 C}{\partial Y^2} + \frac{D_T}{T_\infty}\frac{\partial^2 T}{\partial Y^2} \right), \tag{32}$$

$$k(T) = \frac{k_{nf}}{(\rho C_p)_{nf}} (T_w - T_\infty)^{1-n} U_w^{n-1} \left| \frac{\partial T}{\partial Y} \right|^{n-1}. \tag{33}$$

The boundary conditions are as follows,

$$T(X,0) = T_w + k_{nf}(T_w - T_\infty)^{1-n} \left| \frac{\partial T}{\partial Y} \right|^{n-1} \frac{\partial T}{\partial Y}|_{y=0}, \tag{34}$$

$$C(X,0) = C_w, T(X,\infty) = T_\infty, C(X,\infty) = C_\infty, \tag{35}$$

where T shows temperature in the boundary layer, T_∞ denotes the temperature away from the sheet and is a constant, and T_w indicates the unified temperature of the fluid. C is the concentration of the fluid, C_∞ is the fluid concentration in the free stream, and C_w the unified concentration of the fluid.

For the sake of gaining the similarity solutions of equations, the following similarity variables are introduced,

$$\theta(\eta) = \frac{T - T_\infty}{T_w - T_\infty}, \phi(\eta) = \frac{C - C_\infty}{C_w - C_\infty}. \tag{36}$$

Then, Equations (31)–(33) become

$$n\varphi_4 \theta'' |\theta'|^{n-1} + \frac{2mn - m + 1}{n+1} Pr \varphi_3 f \theta' + PrNb\varphi_3 \phi' \theta' + PrNt\varphi_3 \theta'^2 = 0, \tag{37}$$

$$\phi'' + \frac{2mn + 1 - m}{n+1} Scf\phi' + \frac{Nt}{Nb}\theta'' = 0. \tag{38}$$

The boundary conditions Equations (34) and (35) are converted to

$$\theta(0) = 1 + \beta\theta'(0)|\theta'(0)|^{n-1}, \quad \theta(\infty) = 0, \tag{39}$$

$$\phi(0) = 1, \quad \phi(\infty) = 0, \tag{40}$$

where Pr denotes Prandtl number, Nt represents thermophoresis parameter, Sc is Schmidt number, and Nb is Brownian motion parameter. The above parameters, φ_3, φ_4, and β, are defined as

$$Pr = \frac{\mu_f}{\alpha_f}, Nb = \frac{\tau D_B (C_w - C_\infty)}{\mu_f}, Nt = \frac{\tau D_T (T_w - T_\infty)}{\mu_f T_\infty}, \tag{41}$$

$$\varphi_3 = 1 - \varphi + \varphi \frac{(\rho C_p)_s}{(\rho C_p)_f}, \varphi_4 = \frac{k_s + 2k_f - 2\varphi(k_f - k_s)}{k_s + 2k_f + \varphi(k_f - k_s)}, \tag{42}$$

$$\beta = \frac{k_{nf}}{\mu_{nf}^{\frac{n}{n+1}}} (C^{2n-1} X^{2mn-n-m})^{\frac{1}{n+1}}, Sc = \frac{\mu_f}{D_B}. \tag{43}$$

Momentous physical parameters are expressible as follows,

$$C_f = \frac{\mu_{nf} |\frac{\partial u}{\partial y}|^{n-1} \frac{\partial u}{\partial y}|_{y=0}}{\frac{1}{2}\rho_f u_w^2} = \frac{|f''(0)|^{n-1} f''(0)}{(1-\varphi)^{2.5}} Re_x^{-\frac{1}{n+1}}, \tag{44}$$

$$C_f Re_x^{-\frac{1}{n+1}} = \frac{|f''(0)|^{n-1} f''(0)}{(1-\varphi)^{2.5}}, \tag{45}$$

$$Nu_x = -\frac{x k_{nf} \frac{\partial T}{\partial y}|_{y=0}}{k_f (T_w - T_\infty)} = -\frac{k_s + 2k_f - 2\varphi(k_f - k_s)}{k_s + 2k_f + \varphi(k_f - k_s)} Re_x^{\frac{1}{n+1}} \theta'(0), \tag{46}$$

$$Nu_x Re_x^{-\frac{1}{n+1}} = -\frac{k_s + 2k_f - 2\varphi(k_f - k_s)}{k_s + 2k_f + \varphi(k_f - k_s)} \theta'(0), \tag{47}$$

$$Sh_x = -\frac{x D_B \frac{\partial C}{\partial y}|_{y=0}}{D_B (C_w - C_\infty)} = -Re_x^{\frac{1}{n+1}} \phi'(0), \tag{48}$$

$$Sh_x Re_x^{-\frac{1}{n+1}} = -\phi'(0). \tag{49}$$

3. Solution Procedures

In this section, the homotopy analysis method (HAM) [29] is used to solve this problem. The initial guess solutions of velocity, temperature, and concentration, based on boundary conditions, are, respectively,

$$f_0 = B_1 + B_2 e^{-\eta} + B_3 \eta, \theta_0 = B e^{-\eta}, \phi_0 = e^{-\eta}. \tag{50}$$

Three linear operators are selected as

$$L_f = f''' + f'', L_\theta = \theta'' + \theta', L_\phi = \phi'' - \phi. \tag{51}$$

These operators satisfy some properties:

$$L_f (C_1 + C_2 e^{-\eta} + C_3 \eta) = 0, L_\theta (C_4 e^{-\eta} + C_5) = 0, L_\phi (C_6 e^{-\eta} + C_7 e^{\eta}) = 0 \tag{52}$$

where $C_i (i = 1, 2, \cdots, 7)$ are arbitrary constants.

The 0-th order deformation equations and its boundary conditions are derived and the expressions are written as

$$(1-p) L[F(\eta, p) - f_0(\eta)] = p h_f H_f(\eta) N_f[F(\eta, p)], \tag{53}$$

$$(1-p) L[\Theta(\eta, p) - \theta_0(\eta)] = p h_\theta H_\theta(\eta) N_\theta[F(\eta, p), \Theta(\eta, p), \Phi(\eta, p)], \tag{54}$$

$$(1-p) L[\Phi(\eta, p) - \phi_0(\eta)] = p h_\phi H_\varphi(\eta) N_\phi[F(\eta, p), \Theta(\eta, p), \Phi(\eta, p)]; \tag{55}$$

$$F(0,p)=0, F'(\infty,p)=d, \Theta(\infty,p)=0, \Phi(0,p)=1, \Phi(\infty,p)=0, \tag{56}$$

$$F'(0,p)=1+\lambda_1 F''(0,p)+\lambda_2 F'''(0,p)+\lambda_3|F''(0,p)|^{n-1}F''(0,p), \tag{57}$$

$$\Theta(0,p)=1+\beta\Theta_0{}'(0,p)|\Theta_0{}'(0,p)|^{n-1}. \tag{58}$$

In the above equations, $p\in[0,1]$ is the embedding parameter; h_f, h_θ, and h_ϕ are auxiliary non-zero parameters; and $H_f(\eta)$, $H_\theta(\eta)$, and $H_\varphi(\eta)$ are nonzero auxiliary functions [30]. Obviously, for $p=0$ and $p=1$, we have

$$\begin{array}{ll} F(\eta,0)=f_0(\eta), & F(\eta,1)=f(\eta), \\ \Theta(\eta,0)=\theta_0(\eta), & \Theta(\eta,1)=\theta(\eta), \\ \Phi(\eta,0)=\phi_0(\eta), & \Phi(\eta,1)=\phi(\eta). \end{array} \tag{59}$$

As p increases from 0 to 1, $F(\eta,p)$ is from the initial guess $f_0(\eta)$ to the exact solution $f(\eta)$, $\Theta(\eta,p)$ is from the initial guess $\theta_0(\eta)$ to the exact solution $\theta(\eta)$, and $\Phi(\eta,p)$ is from the initial guess $\phi_0(\eta)$ to the exact solution $\phi(\eta)$ [30]. With Taylor's theorem, they can write

$$F(\eta,p) = F(\eta,0)+\sum_{k=1}^{+\infty} f_k(\eta)p^k, f_k(\eta)=\frac{1}{k!}\frac{\partial^k F(\eta,p)}{\partial p^k}|_{p=0}, \tag{60}$$

$$\Theta(\eta,p) = \Theta(\eta,0)+\sum_{k=1}^{+\infty} \theta_k(\eta)p^k, \quad \theta_k(\eta)=\frac{1}{k!}\frac{\partial^k \Theta(\eta,p)}{\partial p^k}|_{p=0}. \tag{61}$$

$$\Phi(\eta,p) = \Phi(\eta,0)+\sum_{k=1}^{+\infty} \phi_k(\eta)p^k, \quad \phi_k(\eta)=\frac{1}{k!}\frac{\partial^k \Phi(\eta,p)}{\partial p^k}|_{p=0}. \tag{62}$$

Assuming that the auxiliary parameters h_f, h_θ, and h_ϕ are appropriate chosen, we can obtain convergent solutions in the following form.

$$f(\eta)=f_0(\eta)+\sum_{k=1}^{\infty} f_k(\eta), \theta(\eta)=\theta_0(\eta)+\sum_{k=1}^{\infty}\theta_k(\eta), \phi(\eta)=\phi_0(\eta)+\sum_{k=1}^{\infty}\phi_k(\eta). \tag{63}$$

For the sake of getting the higher order deformation equation, differentiating the 0-th order deformation Equations (53)–(55) k times with regard to p, set $p=0$ and divide by $k!$, to attain

$$L_f(f_k(\eta)-\chi_k f_{k-1}(\eta))=h_f H_f(\eta)R_{f,k}(\eta), \tag{64}$$

$$L_\theta(f_\theta(\eta)-\chi_\theta f_{\theta-1}(\eta))=h_\theta H_\theta(\eta)R_{\theta,k}(\eta), \tag{65}$$

$$L_\phi(f_\phi(\eta)-\chi_\phi f_{\phi-1}(\eta))=h_\phi H_\phi(\eta)R_{\phi,k}(\eta), \tag{66}$$

where $R_{f,k}(\eta)$, $R_{\theta,k}(\eta)$, and $R_{\phi,k}(\eta)$ are, respectively,

$$\begin{aligned} & R_{f,k}(\eta) \\ &= \chi_k \sum_{l=0}^{k-2} f_l''' \sum_{j=2}^{k-l} \sum_{\substack{i_1+i_2+\cdots i_{k-1}=j-1 \\ i_1+2i_2+\cdots+(k-1)i_{k-1}=k-1-l}}^{k-1} \frac{n(n-1)\cdots(n-j+1)}{i_1!i_2!\cdots i_{k-1}!}|f_0''|^{n-j}\prod_{q=1}^{k-1}|f_q''|^{i_q} \\ &+ n f_{k-1}'''|f_0''|^{n-1} - m\varphi_1\varphi_2\sum_{i=0}^{k-1} f_i' f_{k-1-i}' \\ &+ \varphi_1\varphi_2\tfrac{2mn-m+1}{n+1}\sum_{i=0}^{k-1} f_i f_{k-1-i}'' - \varphi_1 M f_{k-1}', \end{aligned} \tag{67}$$

$$\begin{aligned} & R_{\theta,k}(\eta) \\ &= \chi_k \sum_{l=0}^{k-2} \theta_l'' \sum_{j=2}^{k-l} \sum_{\substack{i_1,i_2,\cdots i_k=0 \\ i_1+i_2+\cdots+i_{k-1}=j-1 \\ i_1+2i_2+\cdots+(k-1)i_{k-1}=k-1-l}}^{k-1} \frac{n(n-1)\cdots(n-j+1)\varphi_4}{i_1!i_2!\cdots i_{k-1}!} |\theta_0'|^{n-j} \prod_{q=1}^{k-1} |\theta_q'|^{i_q} \\ &+ n\varphi_4 \theta_{k-1}'' |\theta_0'|^{n-1} + \frac{2mn-m+1}{n+1} \Pr \varphi_3 \sum_{i=0}^{k-1} f_i \theta_{k-1-i}' \\ &+ \Pr Nb \varphi_3 \sum_{i=0}^{k-1} \phi_i \theta_{k-1-i}' + \Pr Nt \varphi_3 \sum_{i=0}^{k-1} \theta_i' \theta_{k-1-i}', \end{aligned} \tag{68}$$

$$R_{\phi,k}(\eta) = \phi_{k-1}'' + \frac{2mn+1-m}{n+1} Sc \sum_{i=0}^{k-1} f_i \phi_{k-1-i}' + \frac{Nt}{Nb} \theta_{k-1}'', \tag{69}$$

$$\chi_k = \begin{cases} 0 & k \le 1, \\ 1 & k > 1. \end{cases} \tag{70}$$

Boundary conditions Equations (56)–(58) become

$$f_k(0) = 0, f_k'(\infty) = 0, \theta_k(\infty) = 0, \phi_k(0) = 0, \phi_k(\infty) = 0, \tag{71}$$

$$\begin{aligned} & f_k'(0) \\ &= \sum_{l=0}^{k-1} f_l''(0) \sum_{j=2}^{k+1-l} \sum_{\substack{i_1,i_2,\cdots i_k=0 \\ i_1+i_2+\cdots+i_k=j-1 \\ i_1+2i_2+\cdots+ki_k=k-l}}^{k} \frac{\lambda_3(n-1)(n-2)\cdots(n-j+1)}{i_1!i_2!\cdots i_k!} |f_0''(0)|^{n-j} \prod_{q=1}^{k} |f_q''(0)|^{i_q} \\ &+ \lambda_3 f_k''(0) |f_0''(0)|^{n-1} + \lambda_1 f_k''(0) + \lambda_2 f_k'''(0), \end{aligned} \tag{72}$$

$$\begin{aligned} & \theta_k(0) \\ &= \sum_{l=0}^{k-1} \theta_l'(0) \sum_{j=2}^{k+1-l} \sum_{\substack{i_1,i_2,\cdots i_k=0 \\ i_1+i_2+\cdots+i_k=j-1 \\ i_1+2i_2+\cdots+ki_k=k-l}}^{k} \frac{\beta(n-1)(n-2)\cdots(n-j+1)}{i_1!i_2!\cdots i_k!} |\theta_0'(0)|^{n-j} \prod_{q=1}^{k} |\theta_q'(0)|^{i_q} \\ &+ \beta \theta_k'(0) |\theta_0'(0)|^{n-1}. \end{aligned} \tag{73}$$

4. Results and Discussion

In homotopy analysis, the h-curves are ploted to select the effective region of parameter h. For the sake of obtaining the convergent parameters h_f, h_θ, and h_ϕ, Figures 1–3 plot the h-curves of various orders for $f''(0)$, $\theta(0)$ and $\phi(0)$. Ranges of h-curves are $[-0.4, 0]$, $[-0.5, -0.3]$, $[-0.5, 0.3]$, that is, the horizontal segment of the curves, which is called the effective region, so $h_f = h_\theta = h_\phi = h = -0.35$ is selected in the paper.

For the sake of proving the accuracy and effectiveness of homotopy analysis after determining values of h_f, h_θ, and h_ϕ, Figure 4 plots the error curves of various power law index by the "BVPh2.0" procedure software package. As can be seen from Figure 4, the errors have reached 10^{-4} in the second order, meeting the standards of engineering calculation. The larger the order, the smaller the error becomes. Further, surface friction coefficients are compared with the literature [31] for various first-order slip parameter λ_1 in Table 3.

Table 2. The physical capabilities of base fluid and nanoparticles [26].

	Base Fluid (0.0–0.4%)	***Cu***
$C_p/(\mathrm{J}\cdot \mathrm{kg}^{-1}\cdot \mathrm{K}^{-1})$	4179	385
$\rho/(\mathrm{kg}\cdot \mathrm{m}^{-3})$	997.1	8933
$k/(\mathrm{W}\cdot \mathrm{m}^{-1}\cdot \mathrm{K}^{-1})$	0.613	400
$\sigma/(\Omega^{-1}\cdot \mathrm{m}^{-1})$	0.05	5.96×10^7

Table 3. Comparisons of $C_f R_e^{\frac{1}{n+1}}$ for various λ_1 as $n = 1$, $m = 1$, $d = 1.5$, $\lambda_2 = \lambda_3 = 0$, $\varphi = 0$.

λ_1	$C_f R_e^{\frac{1}{2}}$		
	Ul Haq et al. [31]	**Present Research**	**Percent Difference**
0.5	0.34153	0.341678	0.043%
1	0.34153	0.341215	0.092%

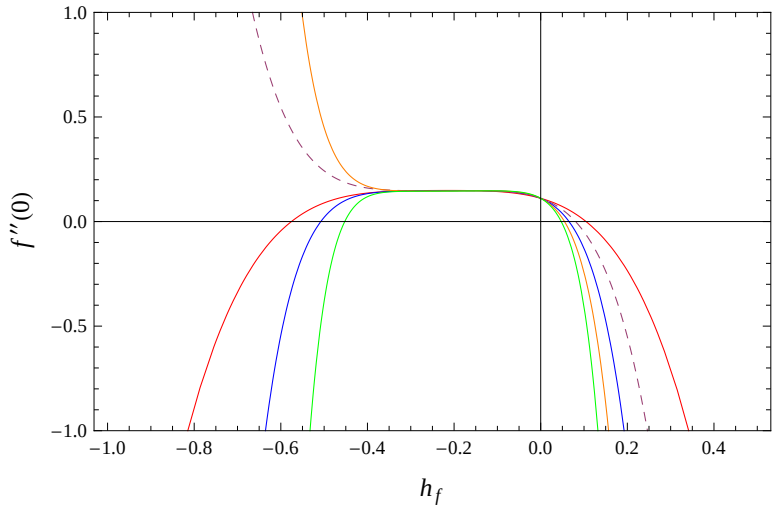

Figure 1. h_f-curves.

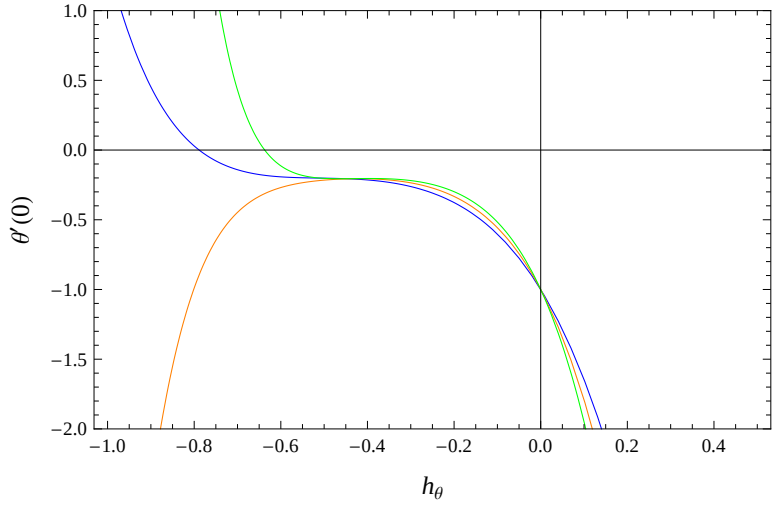

Figure 2. h_θ-curves.

After attesting the accuracy and effectiveness of homotopy analysis, the impacts of various physical parameters are analyzed, such as nondimensional velocity $f'(\eta)$, temperature $\theta(\eta)$, etc.

Meanwhile, the flow of power law nanofluid is numerically simulated by the widely used software Ansys Fluent to further explore the flow properties.

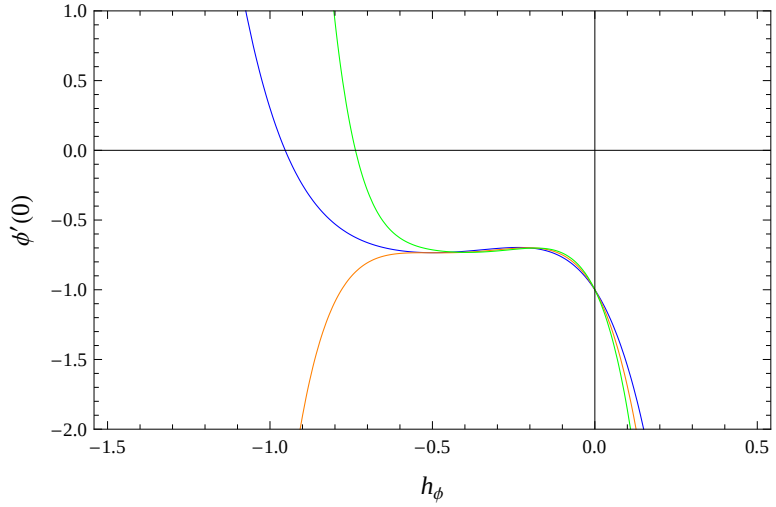

Figure 3. h_ϕ-curves.

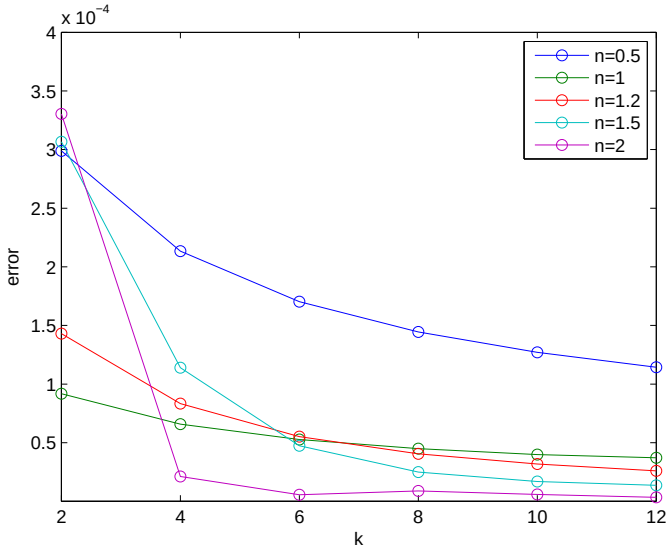

Figure 4. Total error of approximation for various powers n.

4.1. Behavior of Velocity Profiles

Figures 5 and 6 demonstrate effects of power law exponential of the plate m and Hartmann number M on nondimensional velocity $f'(\eta)$. The velocity distribution for various m is showed in Figure 5. By increasing the power exponent of the plate m, the tensile speed of the plate increases. Greater deformation is effected in the fluid, leading to the increase of $f'(\eta)$. As pointed out in [32], the effects of M on $f'(\eta)$ are visible in Figure 5. Recall that Hartmann number M expresses the ratio of electromagnetic force to viscous force. Due to the fact that greater Hartmann number corresponds to larger Lorenz force, the velocity $f'(\eta)$ increases.

When the fluid is pseudoplastic and expansive, impacts of d on $f'(\eta)$ are illustrated in Figure 7. In Figure 7, the velocity of the fluid has upward tendency for various d. Whereas, the velocity of expansive fluid increases slower than that of pseudoplastic fluid due to the increase of the fluid viscosity.

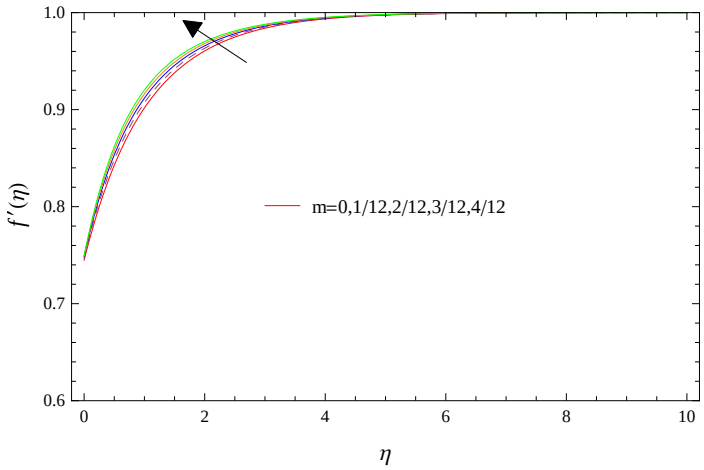

Figure 5. Impacts of m on $f'(\eta)$.

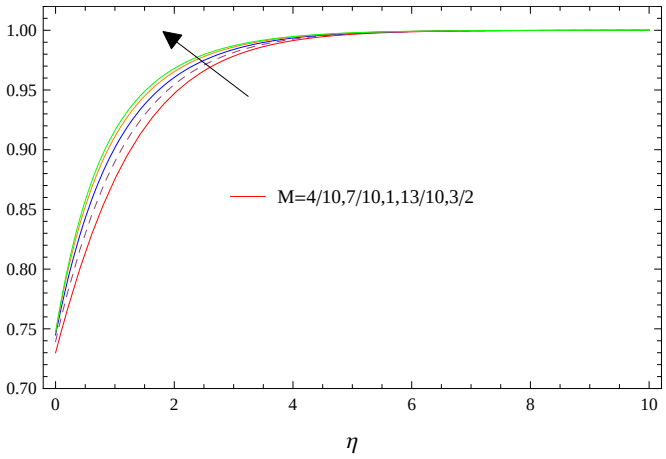

Figure 6. Impacts of M on $f'(\eta)$.

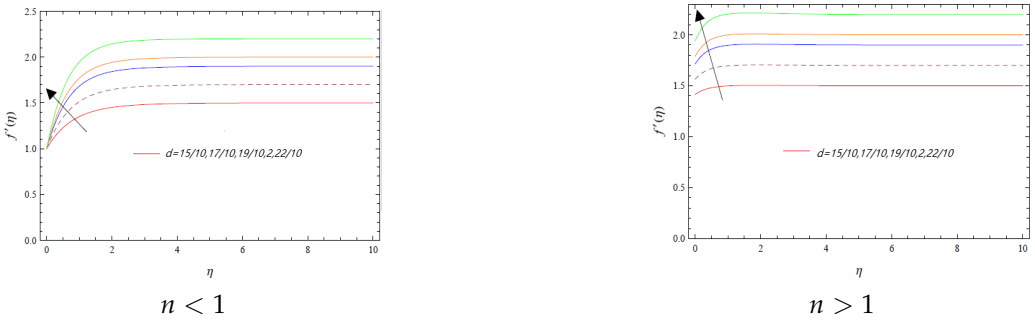

$n < 1$ $n > 1$

Figure 7. Impacts of d on $f'(\eta)$ for $n < 1$ and $n > 1$.

Figure 8 clearly presents the impacts of various power law index n on $f'(\eta)$. As seen in Figure 8, the buoyancy becomes larger as the power law index n increases, which causes the increase of velocity.

Influences of different velocity slip parameters λ_1, λ_2, and λ_3 on $f'(\eta)$ are illustrated in Figures 9–11, respectively. Velocity slip mainly affects slip loss and, in a cascade, fluid velocity. With the increases of the second-order slip parameter λ_2, velocity $f'(\eta)$ also increases; however, the results are contradictory when the first-order linear slip parameter λ_1 and nonlinear slip parameter λ_3 increase.

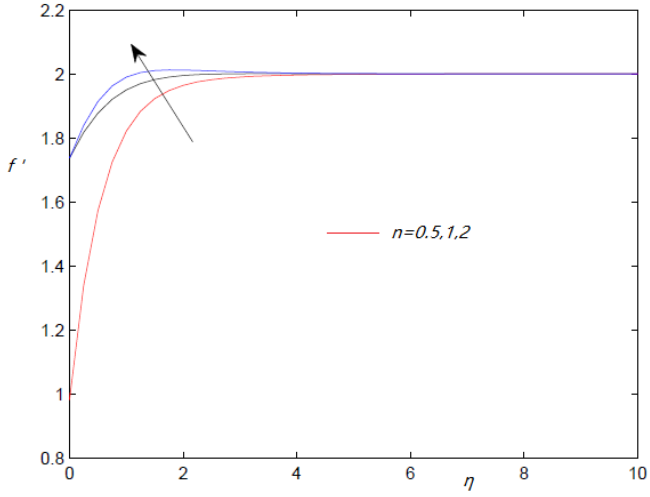

Figure 8. Impacts of n on $f'(\eta)$.

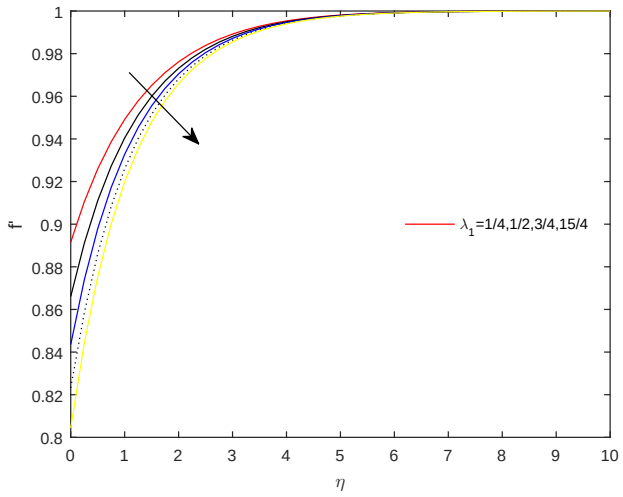

Figure 9. Effects of λ_1 on $f'(\eta)$.

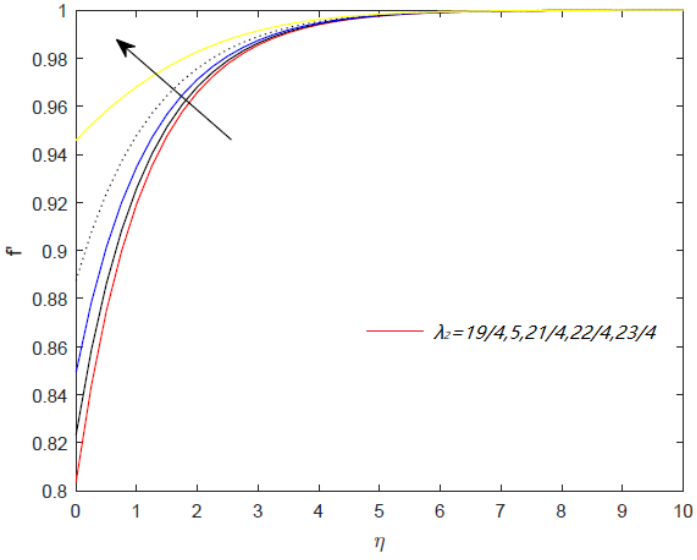

Figure 10. Effects of λ_2 on $f'(\eta)$.

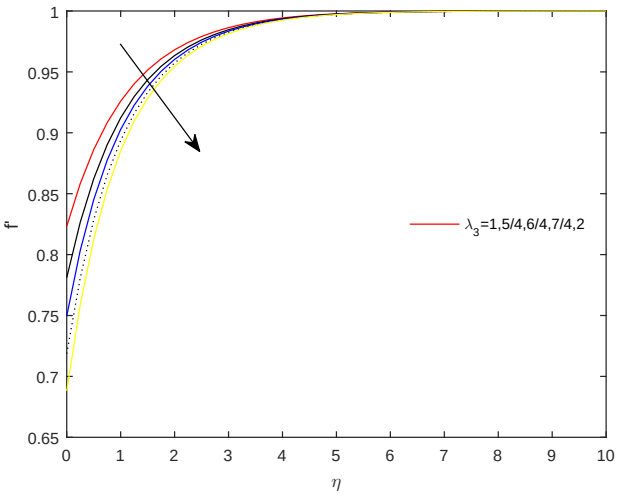

Figure 11. Effects of λ_3 on $f'(\eta)$).

4.2. Behavior of Temperature Profiles

Figures 12 and 13 indicate various temperature behavior for different Nb and Nt. Figure 12 displays the effects of Nb on temperature. Fluid particles generate more heat through random motions when Nb increases, which causes the rise in temperature. Figure 13 clearly shows temperature distribution for various thermophoresis parameter Nt. Thermophoresis indicates that particles move from a high temperature part to a low temperature one in a fluid with temperature gradient. Thus, the temperature increases with the enhancement of the parameter Nt.

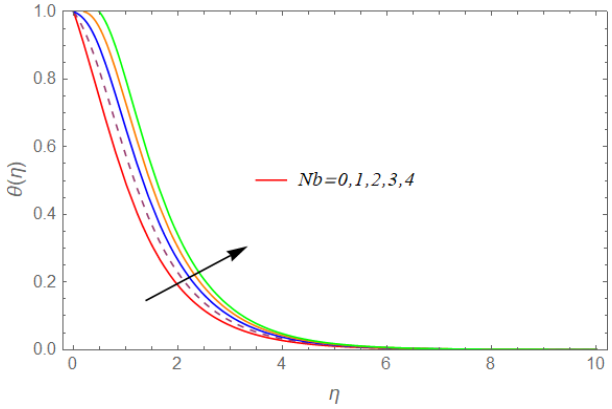

Figure 12. Impacts of Nb on $\theta(\eta)$.

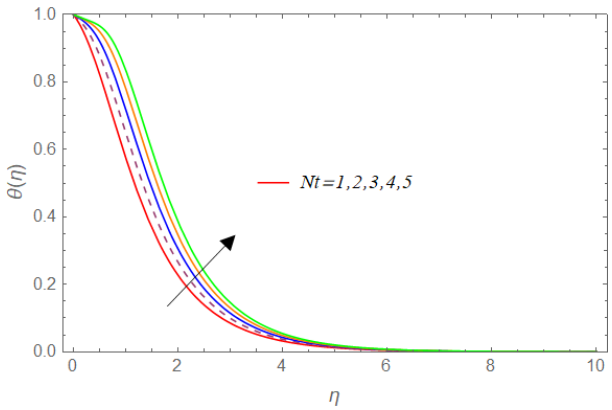

Figure 13. Impacts of Nt on $\theta(\eta)$.

Figures 14 and 15 show temperature distribution for diverse temperature jump parameter β and power law index n. Figure 14 plots the temperature curves for diverse β. Increasing temperature jump parameter β leads to a rise in the thickness of temperature boundary layer. Thus, the temperature has an upward tendency. Figure 15 demonstrates the temperature distribution for various n. The temperature diminish when the power law index rises. In other words, temperature boundary layer becomes thinner with the enhancement of n.

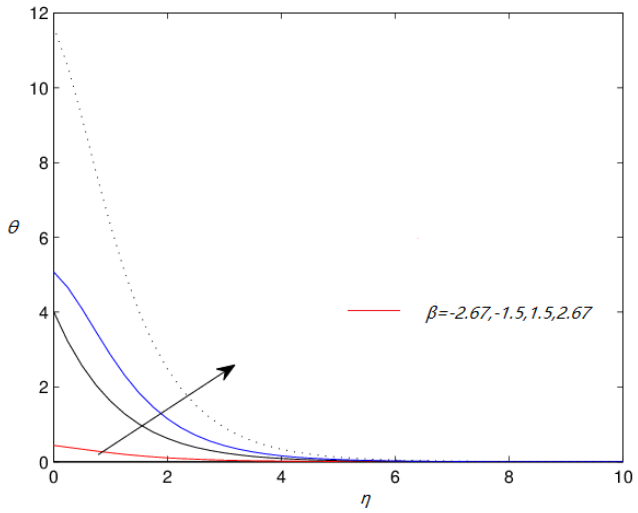

Figure 14. Impacts of β on $\theta(\eta)$.

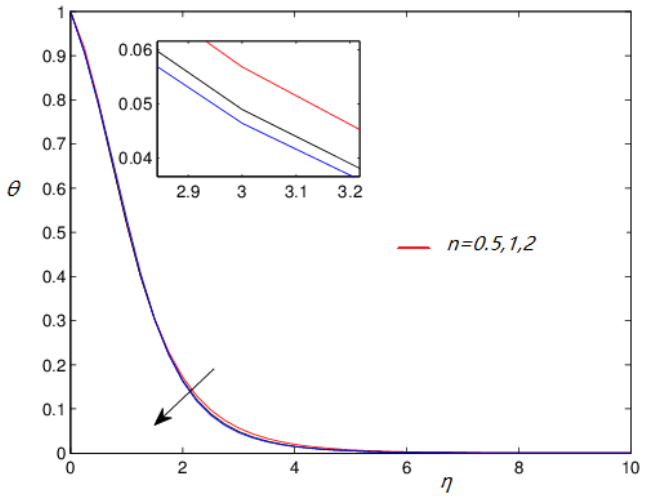

Figure 15. Impacts of n on $\theta(\eta)$.

4.3. Behavior of Concentration Profiles

Figures 16 and 17 show the concentration distribution for diverse values of the Brownian motion parameter Nb and the thermophoresis parameter Nt. From Figure 16, the collision of fluid particles rises with the stronger Brown motion, which leads to the reduction of fluid concentration. Figure 17 indicates the concentration field for various thermophoresis parameter Nt. The magnitude of concentration variation is greater under the influence of thermophoresis parameter.

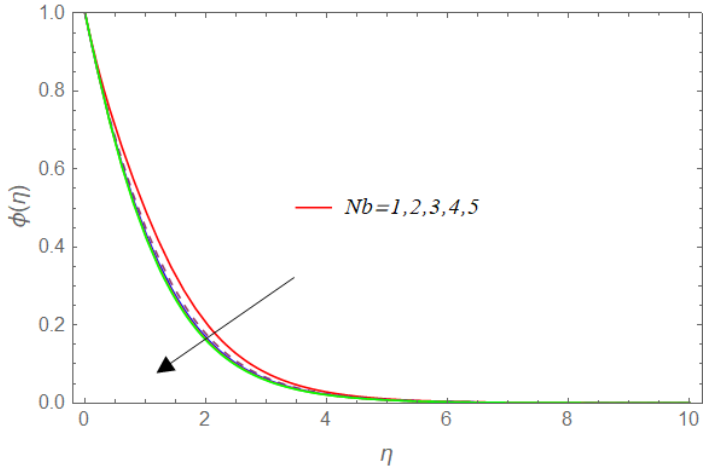

Figure 16. Impacts of Nb on $\phi(\eta)$.

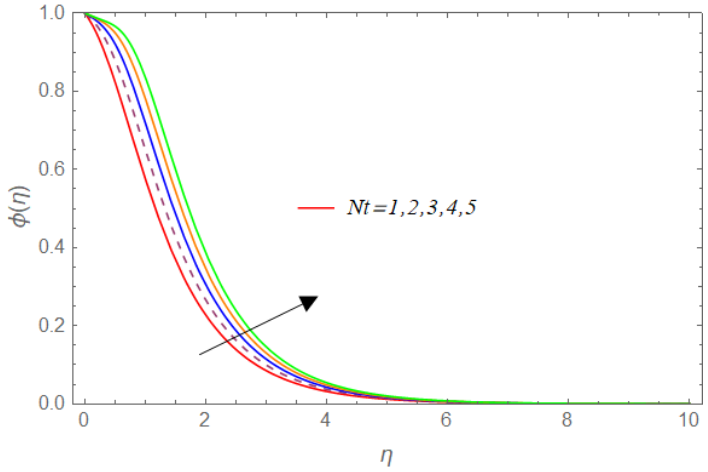

Figure 17. Impacts of Nt on $\phi(\eta)$.

4.4. Analysis of Skin Friction and Nusselt Number

In the study of fluids, vital physical parameters, such as skin friction coefficient and local Nusselt number, are discussed. In this paper, the impacts of various parameters on these two parameters are demonstrated in Table 4. Skin friction coefficients have ascending behavior with the increase of φ, λ_1 and λ_3. On the contrary, the downward trend is seen with the raise of λ_2. For local Nusselt number, when φ and λ_2 rise, the local Nusselt numbers have an upward trend, whereas the local Nusselt numbers diminish with the rise of λ_1, λ_3 and β.

4.5. Simulated Behavior

In this subsection,the laminar model is used to solved governing equations. Ansys Fluent uses the Gauss-–Siedel point-by-point iterative method combined with the algebraic multigrid (AMG) method to solve the algebraic equations. The effects of various parameters on the flow of power-law nanofluid over a stretched thin sheet are simulated. The computational results obtained by using CFD solver are compared with the available results of Chen [33] for some limiting conditions. The present results are proved to be in good agreement as shown in Table 5. The effects of various parameters such as power law exponential of the plate m, nanoparticle volume fraction φ, and power law index n on Nusselt number Nu and skin friction coefficient are shown in Figures 18–22.

Table 4. Effects of φ, λ_1, λ_2, λ_3, and β on $C_f Re_x^{\frac{1}{n+1}}$ and $Nu_x Re_x^{-\frac{1}{n+1}}$ for $n = 1/2$, $m = 0$, $M = 1$, $d = 1$, $Pr = 1$, $Nb = 1$, $Nt = 1$, and $Sc = 1$.

φ	λ_1	λ_2	λ_3	β	$C_f Re_x^{\frac{1}{n+1}}$	$Nu_x Re_x^{-\frac{1}{n+1}}$
0	2	1	1	0	0.499647	0.187766
1.5%	2	1	1	0	0.515072	0.194264
3%	2	1	1	0	0.541362	0.200764
0	1/4	5	1	0	0.28862	0.209897
0	3/4	5	1	0	0.366794	0.209846
0	1	5	1	0	0.396051	0.20919
0	1	5	1	0	0.396051	0.20919
0	1	21/4	1	0	0.359076	0.210207
0	1	22/4	1	0	0.297825	0.210503
0	1	5	1	0	0.396051	0.20919
0	1	5	5/4	0	0.452515	0.201034
0	1	5	6/4	0	0.493526	0.188581
0	2	1	1	0	0.499647	0.187766
0	2	1	1	1.5	0.499647	0.137537
0	2	1	1	8/3	0.499647	0.0804748

Table 5. Comparisons of $C_f R_e^{\frac{1}{n+1}}$ for various n with $m = 0.5$.

n	$C_f R_e^{\frac{1}{n+1}}$		
	Chen [33]	**Present Research**	**Percent Difference**
0.5	−1.831551	−1.831768	0.012%
1	−1.54073	−1.54079	0.003%
1.5	−1.39441	−1.39578	0.098%

The velocity contours for nonlinear slip are simulated in Figure 18. From these diagrams, the flow produces velocity boundary layer near the entrance. Besides, the velocity boundary layer of the pseudoplastic fluid is thicker than that for a Newton and expansive fluid.

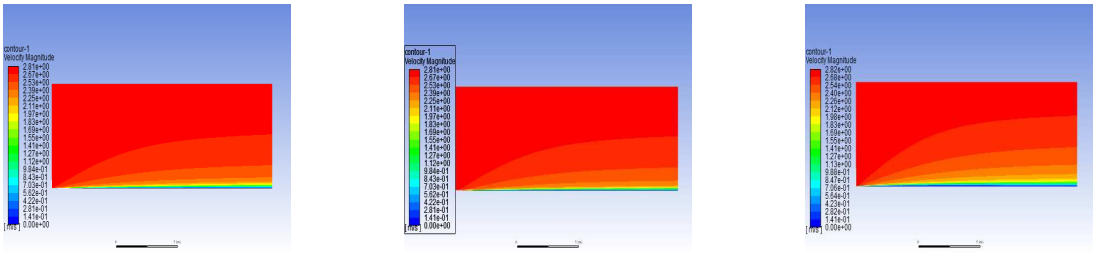

$n = 0.5$ $n = 1$ $n = 1.5$

Figure 18. Velocity contours with $n = 0.5$, $n = 1$, $n = 1.5$.

Figures 19 and 20 present the effect of nanoparticle volume fraction on Nusselt number Nu and skin friction coefficient C_f at fixed values of inlet velocity, power law index. From Figure 19, the local Nusselt number increases at any x-location When nanoparticles are added to the base fluid. This is because a lower local temperature difference between the sheet walls and fluid can be achieved. Therefore, the high thermal conductivity of Cu nanoparticles enhances the thermal performance of the fluid. As the viscosity of the liquid can be increased by adding Cu nanoparticles into the base fluid, the C_f along the thin sheet increases when using higher concentrations of nanoparticles, as shown in Figure 20.

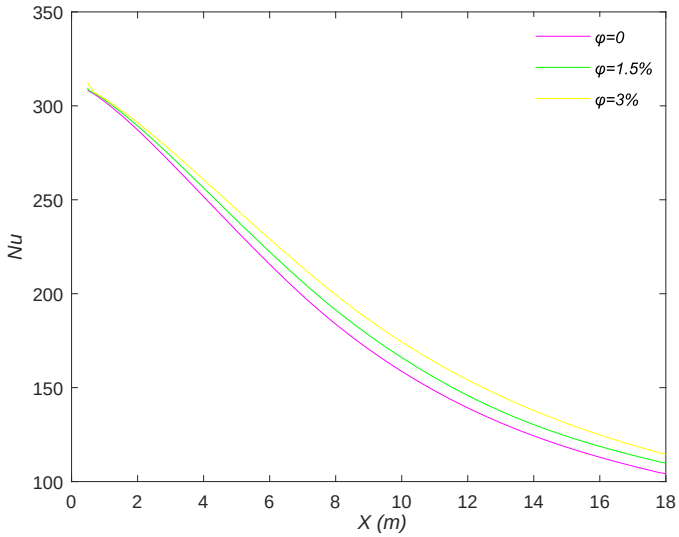

Figure 19. Effect of φ on Nu.

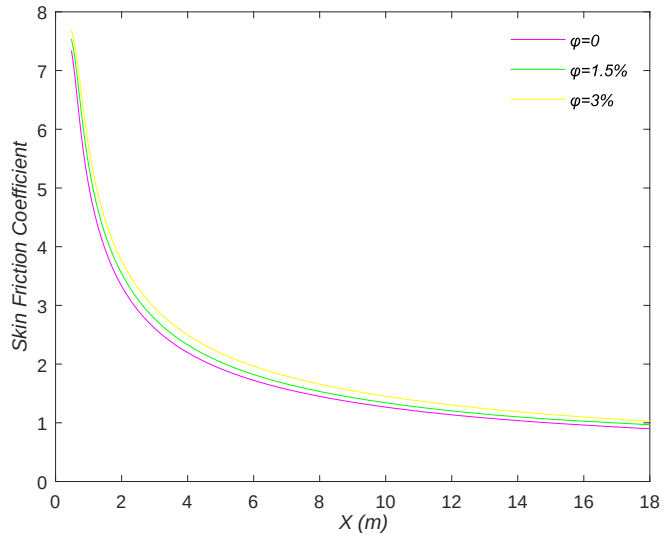

Figure 20. Effect of φ on C_f.

Figure 21 shows the effect of power law index n on skin friction coefficient C_f. The skin friction coefficient decreases with the increase of x-location for a given power law index. However, for a constant x-location, the skin friction coefficient have an upward tendency as the power law index increases.

Figure 22 demonstrates the skin friction coefficient distribution for various φ. The skin friction coefficient increases as the fluid behavior changes from shear-thinning to shear-thickening for a certain φ. As the φ increases the skin friction coefficient increases for a constant power law index.

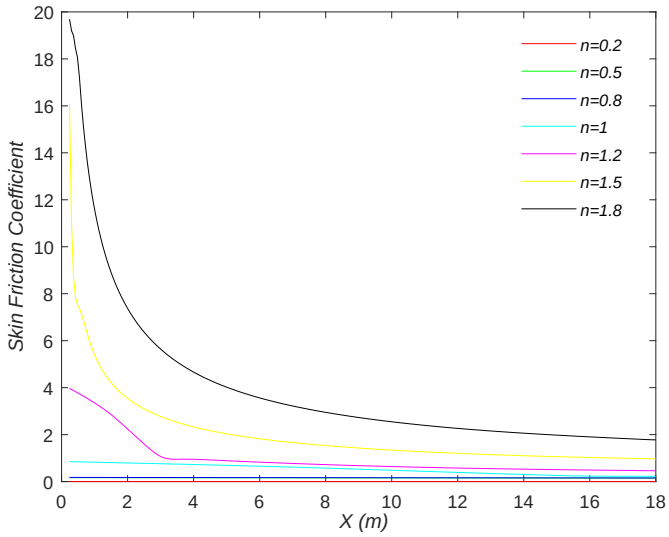

Figure 21. Effect of n on skin friction coefficient.

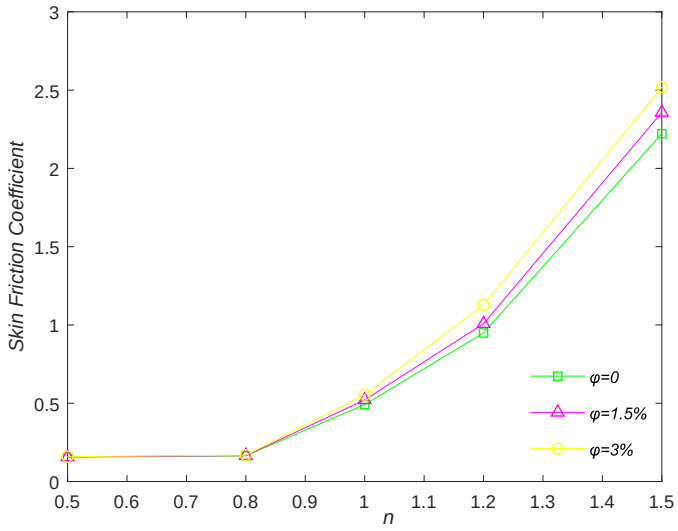

Figure 22. Variation of the skin friction coefficient at different φ.

5. Conclusions

The flow and heat transfer of magnetic nanofluid through a stretched thin sheet with higher-order slip parameters are discussed in the paper. The model contains the influences of Brown motion and thermophoresis impacts. Simplified ODEs are obtained by a series of similarity transformations. The similar solutions are solved through homotopy analysis theory and the stability of the solutions is analyzed. Moreover, the current results are shown to be in good agreement with the literature results, the error of Nusselt number and skin friction coefficient is less than 0.1%. The key conclusions follow.

- Velocity, temperature, and concentration have an upward tendency as the second-order velocity slip parameter, thermophoresis parameter, and temperature jump parameter increase, but a downward trend like the first-order linear slip parameter and nonlinear slip parameters.
- The rise of power law index causes the enhancement of velocity and reduction of temperature.
- Skin friction has increasing behavior due to the enhancement of volume fraction of nanoparticles, the first-order linear slip parameter and nonlinear slip parameter, but decreasing behavior as a result of the second order slip parameter.

- The Nusselt number is found to rise upon the rise of the second order slip parameter, volume fraction, whereas impacts of the first-order linear slip parameter, temperature jump parameter, and nonlinear slip parameter are converse.
- The skin friction coefficient have an upward tendency as the power law index increase at a certain volume fraction of nanoparticles, and also increases as volume fraction of nanoparticles increases at a constant power law index.

Author Contributions: J.Z. conducted the original research, modified the model and contributed analysis tools. X.H. analyzed the data, simulated the modified model and prepared original draft. Y.X. made numerical simulation with ANSYS software. J.Z. and Y.X. revised the manuscript.

Funding: This paper was supported by the National Natural Science Foundation of China (No. 11772046; No. 81870345).

Acknowledgments: The authors would like to express their gratitude to the reviewers for their suggestions.

Conflicts of Interest: The authors declare no conflict of interest.

References

1. Moreira, T.A.; Nascimento, F.J.D.; Ribatski, G. An investigation of the effect of nanoparticle composition and dimension on the heat transfer coefficient during flow boiling of aqueous nanofluids in small diameter channels. *Exp. Therm. Fluid Sci.* **2017**, *89*, 72–89. [CrossRef]
2. Srinivas Rao, S.; Srivastava, A. Whole field measurements to understand the effect of nanoparticle concentration on heat transfer rates in a differentially-heated fluid layer. *Exp. Therm. Fluid Sci.* **2018**, *92*, 326–345. [CrossRef]
3. Ho, M.X.; Pan, C. Experimental investigation of heat transfer performance of molten HITEC salt flow with alumina nanoparticles. *Int. J. Heat Mass Transf.* **2017**, *107*, 1094–1103. [CrossRef]
4. Stephen, U.S.; Choi, J.A.E. Enhancing thermal conductivity of fluids with nanoparticles. *ASME Int. Mech. Eng. Congr. Exp.* **1995**, *66*, 99–105.
5. Sheremet, M.A.; Trimbitas, R.; Grosan, T.; Pop, I. Natural convection of an alumina-water nanofluid inside an inclined wavy-walled cavity with a non-uniform heating using Tiwari and Das′ nanofluid model. *Appl. Math. Mech.* **2018**, *39*, 1425–1436. [CrossRef]
6. Bowers, J.; Gao, H.; Qiao, G. Flow and heat transfer behavior of nanofluids in microchannels. *Prog. Nat. Sci.* **2018**, *28*, 225–234. [CrossRef]
7. Hamid, A.; Khan, M. Unsteady mixed convective flow of Williamson nanofluid with heat transfer in the presence of variable thermal conductivity and magnetic field. *J. Mol. Liq.* **2018**, *260*, 436–446.
8. Mahdy, A. Simultaneous impacts of MHD and variable wall temperature on transient mixed Casson nanofluid flow in the stagnation point of rotating sphere. *Appl. Math. Mech.* **2018**, *39*, 1327–1340. [CrossRef]
9. Asadi, A.; Aberoumand, S.; Moradikazerouni, A.; Pourfattah, F.; Zyla, G.; Estelle, P.; Mahian, O.; Wongwises, S.; Nguyen, H.M.; Arabkoohsar, A. Recent advances in preparation methods and thermophysical properties of oil-based nanofluids: A state-of-the-art review. *Powder Technol.* **2019**, *352*, 209–226. [CrossRef]
10. Pourfatta, H.F.; Arani, A.A.A.; Babaie, M.R.; Nguyen, H.M.; Asadi, A. On the thermal characteristics of a manifold microchannel heat sink subjected to nanofluid using two-phase flow simulation. *Int. J. Heat Mass Transf.* **2019**, *143*, 1–13. [CrossRef]
11. Alarifi, I.M.; Alkouh, A.B.; Ali, V.; Nguyen, H.M.; Asadi, A. On the rheological properties of MWCNT-TiO2/oil hybrid nanofluid: An experimental investigation on the effects of shear rate, temperature, and solid concentration of nanoparticles. *Powder Technol.* **2019**, *355*, 157–162. [CrossRef]
12. Javanbakh, T.M.; Moosavi, A. Heat transfer on topographically structured surfaces for power law fluids. *Int. J. Heat Mass Transfer* **2018**, *121*, 857–871. [CrossRef]
13. Turan, O.; Yigit, S.; Liang, R.; Chakraborty, N. Laminar mixed convection of power-law fluids in cylindrical enclosures with heated rotating top wall. *Int. J. Heat Mass Transf.* **2018**, *124*, 885–899. [CrossRef]
14. Zhang, H.; Kang, Y.; Xu, T. Study on Heat Transfer of Non-Newtonian Power Law Fluid in Pipes with Different Cross Sections. *Procedia Eng.* **2017**, *205*, 3381–3388. [CrossRef]
15. Ahmed, F.; Iqbal, M. MHD power law fluid flow and heat transfer analysis through Darcy Brinkman porous media in annular sector. *Int. J. Mech. Sci.* **2017**, *130*, 508–517. [CrossRef]

16. Khan, M.; Hafeez, A. A review on slip-flow and heat transfer performance of nanofluids from a permeable shrinking surface with thermal radiation: Dual solutions. *Chem. Eng. Sci.* **2017**, *173*, 1–11. [CrossRef]
17. Ramya, D.; Raju, R.S.; Rao, J.A. Effects of velocity and thermal wall slip on magnetohydrodynamics (MHD) boundary layer viscous flow and heat transfer of a nanofluid over a non-linearly-stretching sheet: A numerical study. *Propuls. Power Res.* **2018**, *7*, 182–195. [CrossRef]
18. Abbas, N.; Saleem, S.; Nadeem, S. On stagnation point flow of a micro polar nanofluid past a circular cylinder with velocity and thermal slip. *Results Phys.* **2018** *9*, 1224–1232. [CrossRef]
19. Usman, M.; Soomro, F.A.; Ul Haq, R. Thermal and velocity slip effects on Casson nanofluid flow over an inclined permeable stretching cylinder via collocation method. *Int. J. Heat Mass Transf.* **2018**, *122*, 1255–1263. [CrossRef]
20. Jayachandra Badu, M.; Sandeep, N. Three-dimensional MHD slip flow of nanofluids over a slendering stretching sheet with thermophoresis and Brownian motion effects. *Adv. Powder Technol.* **2016**, *27*, 2039–2050. [CrossRef]
21. Beskok, A.; Karniadakis, G.E. Rarefaction and compressibility effects in gas microflows. *J. Fluids Eng.* **1996**, *118*, 448–456. [CrossRef]
22. Uddin, M.J.; Khan, W.A.; Ismail, A.I.M. Melting and second order slip effect on convective flow of nanofluid past a radiating stretching/shrinking sheet. *Propuls. Power Res.* **2018**, *7*, 60–71. [CrossRef]
23. Kamran, M.; Wiwatanaoataphee, B. Chemical reaction and Newtonian heating effects on steady convection flow of a micropolar fluid with second order slip at the boundary. *Eur. J. Mech.-B/Fluids* **2018**, *71*, 138–150. [CrossRef]
24. Farooq, S.; Hayat, T.; AlsaedI; A; Ahmad, B. Numerically framing the features of second-order velocity slip in mixed convective flow of Sisko nanomaterial considering gyrotactic microorganisms. *Int. J. Heat Mass Transf.* **2017**, *112*, 521–532. [CrossRef]
25. Yasin, M.H.M.; Ishak, A.; Pop, I. Boundary layer flow and heat transfer past a permeable shrinking surface embedded in a porous medium with a second-order slip: A stability analysis. *Appl. Therm. Eng.* **2017**, *115*, 1407–1411. [CrossRef]
26. Mustafa, M.; Khan, J.A. Numerical study of partial slip effects on MHD flow of nanofluids near a convectively heated stretchable rotating disk. *J. Mol. Liq.* **2017**, *234*, 287–295. [CrossRef]
27. Hayat, T.; Ijaz, M.; Qayyum, S.; Ayub, M.; Alsaedi, A. Mixed convective stagnation point flow of nanofluid with Darcy-Fochheimer relation and partial slip. *Results Phys.* **2018**, *9*, 771–778. [CrossRef]
28. Mitsuya, Y. Modified Reynolds Equation for Ultra-Thin Film Gas Lubrication Using 1.5-Order Slip-Flow Model and Considering Surface Accommodation Coefficient. *J. Tribol.* **1993**, *115*, 289–294. [CrossRef]
29. Liao, S.J. *Homotopy Analysis Method in Nonlinear Differential Equations*; Shanghai Jiao Tong University: Shanghai, China, 2012.
30. Zhu, J.; Zheng, L.C.; Zhang, X.X. Analytical solution to stagnation-point flow and heat transfer over a stretching sheet based on homotopy analysis. *Appl. Math. Mech.* **2009**, *30*, 463–474. [CrossRef]
31. Ul Haq, R.; Nadeem, S.; Khan, Z.H.; Akbar, N.S. Thermal radiation and slip effects on MHD stagnation point flow of nanofluid over a stretching sheet. *Phys. E Low-Dimens. Syst. Nanostruct.* **2015**, *65*, 17–23. [CrossRef]
32. Lin, Y.H.; Zheng, L.C.; Li, B.T.; Ma, L.X. A new diffusion for laminar boundary layer flow of power law fluids past a flat surface with magnetic effect and suction or injection. *Int. J. Heat Mass Transf.* **2015**, *90*, 1090–1097. [CrossRef]
33. Chen, C.H. Effects of magnetic field and suction/injection on convection heat transfer of non-Newtonian power-law fluids past a power-law stretched sheet with surface heat flux. *Int. J. Therm. Sci.* **2008**, *47*, 954–961. [CrossRef]